10-2020

A Framework for Pore-Scale Simulation of Effective Electrical Conductivity and Permittivity of Porous Media in the Frequency Range From 1 mHz to 1 GHz

Qifei Niu
Boise State University

Chi Zhang
University of Kansas

Manika Prasad
Colorado School of Mines

A Framework for Pore-Scale Simulation of Effective Electrical Conductivity and Permittivity of Porous Media in the Frequency Range From 1 mHz to 1 GHz

Qifei Niu[1] [iD]**, Chi Zhang[2]** [iD]**, and Manika Prasad[3]**

[1]Department of Geosciences, Boise State University, Boise, ID, USA, [2]Department of Geology, The University of Kansas, Lawrence, KS, USA, [3]Department of Geophysics, Colorado School of Mines, Golden, CO, USA

Abstract Geoelectrical methods are broadly used in earth sciences for various purposes. To correctly interpret field geoelectrical data, it is essential to have a mechanistic understanding of the effective electrical conductivity and permittivity of geological materials over a broad frequency range. Recently, the pore-scale numerical simulation, which utilizes the digital microstructural images of the material, has become a powerful tool in studying the effective electrical properties of geological media. However, it is still difficult to incorporate surface-related electrochemical processes in a pore-scale simulation. In this study, we develop a general framework to consider these electrochemical processes in pore-scale simulations, which enable the calculation of broadband effective electrical conductivity and permittivity of porous geological media. A Berea sandstone sample is utilized to demonstrate the use of the proposed framework. Laboratory experiments of the effective electrical conductivity and permittivity of the sample in the frequency range from 10^{-3} to 10^9 Hz provided valuable measurement data for validating the simulation. The good agreement between our simulated spectra and the experimental data provides validation for the numerical simulation to reproduce the variations in the effective electrical conductivity and permittivity of porous geological materials induced by both the electrochemical polarizations and the interfacial polarization. This work thus provides a useful tool for studying the effective electrical properties of porous geological materials featuring complex microstructures.

1. Introduction

Geoelectrical methods are frequently used in earth sciences to study the physical properties and processes of the solid earth (e.g., Kneisel et al., 2008; Knight, 2001; Revil, Karaoulis, et al., 2012; Streich, 2016; Unsworth et al., 2004). Relevant techniques include the electrical resistivity method (Loke et al., 2013), electromagnetic method (Constable, 2010), induced polarization (Kemna et al., 2012), capacitive resistivity method (Kuras et al., 2006), and ground-penetrating radar (Annan, 2005). Such geoelectrical tests provide spatial and/or temporal distribution of the electrical conductivity and/or permittivity of the subsurface. To correctly interpret the geoelectrical measurements, one needs to have a mechanistic understanding of the electrical conduction and polarization in geological materials and their controlling factors such as material microstructure and environmental conditions (e.g., Santamarina et al., 2001).

The electrical conductivity quantifies a material's ability to conduct electric current. For nonmetallic minerals (e.g., quartz), the conductivity is in the order of 10^{-10} S m^{-1} (e.g., Telford et al., 1990), and thus, the solid phase of geological materials is usually considered nonconductive. Pore water in geological materials is conductive due to the electromigration of dissolved ions, and it constitutes the major pathway for the electrical conduction in geological materials. In addition to pore water, the electrical double layer (EDL) forming at the mineral-water interface also conducts electric current (Revil & Glover, 1998), especially in clayey soils and rocks.

The electrical permittivity is associated with a material's ability to store energy (i.e., polarization). The permittivity of water and nonmetallic minerals is usually constant at frequencies lower than ~GHz. The effective permittivity of water-saturated geological materials, however, is frequency dependent and may deviate significantly from the volume-averaged permittivity of its individual phases. As the frequency decreases, the effective permittivity of a geological material generally increases due to the contribution of some pore

or subpore-scale polarizations (e.g., Santamarina et al., 2001). For porous media, several polarization mechanisms have been proposed to explain the frequency-dependent effective electrical permittivity, including the interfacial polarization (Hanai, 1960) and some electrochemical polarizations (see Chelidze & Gueguen, 1999), both of which will be reviewed in section 2.

In principle, the frequency variations in electrical conductivity and permittivity of a material are linked to each other by the principles of causality. Consider a material featuring a spectrum of relaxation times (i.e., characteristic time of polarizations). As the frequency of external electric field decreases, the polarization with larger relaxation times will occur and also contribute to energy storage in the material. This means more energy will be stored from the external field at a lower frequency (i.e., permittivity increases as the frequency decreases). Since the induced electric field in the material during the polarization has a direction opposite to the external electric field, it becomes more difficult for the electric current passing through the material (i.e., the electrical conductivity decreases) if compared to a higher frequency. The causality between both properties means when the electrical permittivity spectrum of a material is known, the electrical conductivity spectrum can be determined accordingly and vice versa. Mathematically, the frequency-dependent conductivity and permittivity can be linked to each other through the Kramers-Kronig relations (e.g., Milton et al., 1997; Volkmann & Klitzsch, 2015).

To study the effective electrical properties of geological materials, the most commonly used approaches are laboratory experiment and theoretical modeling. In the past several decades, these two approaches have been extensively used to develop robust models that can translate measured effective electrical conductivity and permittivity to other physical properties of interest such as porosity and water content (e.g., Lesmes & Friedman, 2005). The most popular model is probably Archie's law (Archie, 1942), which relates the effective electrical conductivity of a porous medium to the pore water conductivity through a power function of the porosity (saturated condition) or volumetric water content (unsaturated condition). Other examples include the differential effective medium theory-based conductivity models (e.g., Sheng, 1990; Sheng & Callegari, 1984) and the empirical Topp's equation (Topp et al., 1980) for high-frequency permittivity (or dielectric permittivity). Recently, significant progress has been made to model the influence of EDL on electrical conduction and polarization in porous media (e.g., see Bairlein et al., 2016; Revil, 2012, 2013; Weller & Slater, 2012).

The effective electrical conductivity and permittivity of geological media are influenced by the material's microstructure (i.e., texture and fabric). While the effect of material texture (e.g., particle/pore size and distribution) has been extensively studied (e.g., Jones & Friedman, 2000), the influence of material fabric (e.g., particle/pore arrangement and orientation) is less explored due to the difficulty of determining microstructural parameters of geological materials. Recently, the pore-scale numerical simulation has emerged as a powerful tool in studying effective properties of soils and rocks (Andrä et al., 2013a, 2013b). In a pore-scale simulation, both microscopic and macroscopic (i.e., effective) properties of the material can be calculated based on the digital microstructural images. Such pore-scale simulations allow us to explore potential relationships between microstructure and effective properties of the material. In addition to pore-scale imaging techniques (e.g., μCT scan or scanning electron microscope; Blunt et al., 2013), numerical experiments such as the discrete element method (Cundall & Strack, 1979) can also be used to generate the digital microstructural images (e.g., Niu et al., 2017; Niu & Zhang, 2018a), opening another way to study microstructural effect on effective electrical properties of geological materials.

Although the pore-scale simulation has been used to study the effective dc conductivity (e.g., Zhan et al., 2010) or high-frequency permittivity (dielectric permittivity) (e.g., Han & Yang, 2018) of porous geological materials, it is still challenging to apply it to studying the electrochemical polarization-induced conductivity/permittivity variations. This is because electrochemical polarizations in porous media are associated with the ion migration and diffusion occurring in a very thin layer (typically from several to tens of nanometers) near the mineral-water interface. A direct simulation of these processes (e.g., Bücker et al., 2019) requires a fine discretization of the sample domain near the mineral-water interface. Considering that the sample volume in a pore-scale simulation is relatively large, ~mm^3, the computational cost of a direct simulation is extremely high. It is therefore desirable to develop new methods that can effectively include electrochemical polarizations in pore-scale simulations.

The objective of this study is to develop such a framework for pore-scale simulations of the broadband effective electrical properties of porous media. For simplicity, in this study, we only consider water-saturated

porous geological media made of nonmetallic minerals. In the following, we first review the theoretical background of electrical conduction and polarization in water-saturated porous media. We then develop the framework for incorporating various electrical polarizations in the pore-scale simulation, including interfacial polarization, membrane polarization, and grain/pore polarization. Finally, we demonstrate the use of our proposed framework by applying it to a Berea sandstone sample.

2. Theoretical Background

2.1. General Definition and Terminology

In this paper, we use the *electrical conductivity* and *electrical permittivity* to describe the electrical properties of a material at a given frequency. Note that the material here can be either a single-phase material (e.g., water) or a composite. Other parameters (such as dc conductivity, dielectric permittivity, complex conductivity, and complex permittivity) have also been seen in geoscience literatures. To avoid confusion, in the following, we define the *electric conductivity* and *electrical permittivity* through the constitutive equations in electromagnetic theory. For composites such as a geological material, the measured electrical properties are essentially average properties of its individual phases (e.g., Torquato, 2013). To distinguish the average properties from the property of individual phases, in this paper, we use the *effective electrical conductivity* and *effective electrical permittivity* to indicate the average (or measured) properties of geological materials.

Assume that a time-varying electric field $\mathbf{E}$ is applied to a material. The induced total current density in the material $\mathbf{J}_t$ is then the sum of the conduction current density $\mathbf{J}_c$ and the displacement current density $\mathbf{J}_d$, expressed as

$$\mathbf{J}_t = \mathbf{J}_c + \mathbf{J}_d. \tag{1}$$

The conduction current density $\mathbf{J}_c$ is related to the applied electric field $\mathbf{E}$ and the dc electrical conductivity σ_{dc} by Ohm's law,

$$\mathbf{J}_c = \sigma_{dc}\mathbf{E}. \tag{2}$$

The displacement current density $\mathbf{J}_d$ is defined as the derivative of the electric displacement field $\mathbf{D}$ respective to time t,

$$\mathbf{J}_d = \partial\mathbf{D}/\partial t. \tag{3}$$

Note that the electrical displacement field $\mathbf{D}$ is related to the electric field $\mathbf{E}$ by

$$\mathbf{D} = \varepsilon_d^*\mathbf{E}, \tag{4}$$

where $\varepsilon_d^* = \varepsilon'_d - i\varepsilon''_d$ (i being the imaginary number) is the complex permittivity of the material excluding ohmic losses. Inserting Equation 4 into Equation 3 and considering the sinusoidal electric field $\mathbf{E} = \mathbf{E}_0\exp(i\omega t)$ yield

$$\mathbf{J}_d = i\omega\varepsilon_d^*\mathbf{E}, \tag{5}$$

where the angular frequency ω is equal to $2\pi f$ (f being the frequency of the external electric field $\mathbf{E}$). Combining Equations 1, 2, and 5 results in

$$\mathbf{J}_t = \left[\sigma_{dc} + i\omega\varepsilon_d^*\right]\mathbf{E}. \tag{6}$$

If we define the complex conductivity σ^* with the equation $\mathbf{J}_t = \sigma^*\mathbf{E}$, we then have

$$\sigma^* = \sigma' + i\sigma'' = (\sigma_{dc} + \omega\varepsilon''_d) + i\omega\varepsilon'_d, \tag{7}$$

where $\sigma' = \sigma_{dc} + \varepsilon''_d$ is the real conductivity and $\sigma'' = \omega\varepsilon'_d$ is the imaginary conductivity of the material. Similarly, if we define complex permittivity with the equation $\mathbf{J}_t = i\omega\varepsilon^*\mathbf{E}$, we will have

$$\varepsilon^* = \varepsilon' - i\varepsilon'' = \varepsilon'_d - i(\varepsilon''_d + \sigma_{dc}/\omega), \tag{8}$$

where ε' and ε'' are the real and imaginary permittivity of the material, respectively. In this study, *electrical conductivity* refers to the real conductivity σ' in Equation 7, and *electrical permittivity* represents the real permittivity ε' in Equation 8. For geological materials, the *effective electrical conductivity* and *permittivity* are indicated by σ'_{eff} and ε'_{eff}, respectively.

2.2. Interfacial Polarization in Heterogeneous Material

In heterogeneous materials, the interfacial polarization (or Maxwell-Wagner polarization, e.g., Olhoeft, 1985) occurs where discontinuity (i.e., interface) separates two phases with different electrical properties. Under an external electric field, the induced electric field normal to the interface in the two phases must be equal. Because of the mismatch of electrical properties, the current density in the two phases at the interface is different, resulting in accumulations of charges at the interface. The induced dipole moment, that is, the interfacial polarization, gives rise to an enhancement of the bulk permittivity of the material if compared to the volume-averaged permittivity of individual phases (e.g., Chen & Or, 2006). In saturated porous media, the relaxation frequency and effective permittivity increment of the interfacial polarization are mainly influenced by the material microstructure and electrical properties of the fluid phase (Bussian, 1983; Samet et al., 2015). There has been a number of theoretical models developed to account for the effect of interfacial polarization on a material's effective electrical properties, including the pioneering work of Maxwell and Wagner (e.g., see Kremer & Schönhals, 2002) and the differential effective medium theory (e.g., Cosenza et al., 2008; Mendelson & Cohen, 1982; Sen et al., 1981). In a pore-scale numerical simulation, however, the electrical discontinuity is naturally considered because of the use of real microstructures (e.g., Toumelin & Torres-Verdín, 2007). Thus, no interfacial polarization models are required in this study.

2.3. Electrochemical Polarizations in Geological Materials

The surface of many geological minerals is negatively charged due to isomorphous substitutions (McBride, 1989) or the presence of hydroxyl group (Zhuravlev, 2000). If immersed in an electrolyte, some ions in the solution will accumulate at the solid-liquid interface to balance the negatively charged mineral surface, forming an ionic cloud, that is, the EDL. The standard EDL model (Hartkamp et al., 2018) describes the structure of the ionic cloud as two distinct layers. In the inner layer (Stern layer), the cations are adsorbed onto the mineral surface due to electrostatic force, and they are immobile in relative to the mineral surface. In the outer diffusive layer, ions are considered as point charges, and the Poisson-Boltzmann equation can be used to describe the distribution of the counterions and electrical potential.

The presence of EDL at the solid-liquid interface can affect both the dc conduction and electrical polarization in porous media. First, because the ion concentration in the EDL is considerably higher than that in the bulk solution, the dc conductivity of the material is enhanced. The conductivity increment, known as the surface conductivity, has been observed in many geological materials, including clays (Revil & Glover, 1998; Rhoades et al., 1976) and even silica sand (Revil et al., 2014). Second, when an external electric field is applied, the EDL can influence the local ion fluxes in the pore space, resulting in an imbalance of cation and anion concentrations at the pore scale. The induced ionic concentration gradient will form an electric dipole moment, and thus, the material is polarized. This polarization is related to electrochemical processes occurring near the solid-liquid interface and thus is termed as *electrochemical polarizations* in this paper. Many models have been developed for electrochemical polarizations in porous media (e.g., Bücker & Hördt, 2013a; Leroy et al., 2008). Based on their microstructural assumptions (see supporting information Text S1), these polarization models can be classified into three groups as shown in Figure 1: grain polarization, pore polarization, and membrane polarization.

2.3.1. Grain Polarization

The grain polarization model assumes that the solid phase of the material is made of grains with regular shapes (e.g., Figure S1b) and that the polarization occurs around these grains (Figure 1a). At the equilibrium state, the ionic concentration in the EDL around the grain reaches a steady state where the electrostatic force is balanced by the thermal diffusion. After applying an external electric field, the ions in and near the EDL will redistribute, and anions (cations) will accumulate on one side and deplete on the other side of the grain. The induced gradient of the ionic concentration imposes an electric dipole moment across the grain, and thus, the electrochemical polarization occurs.
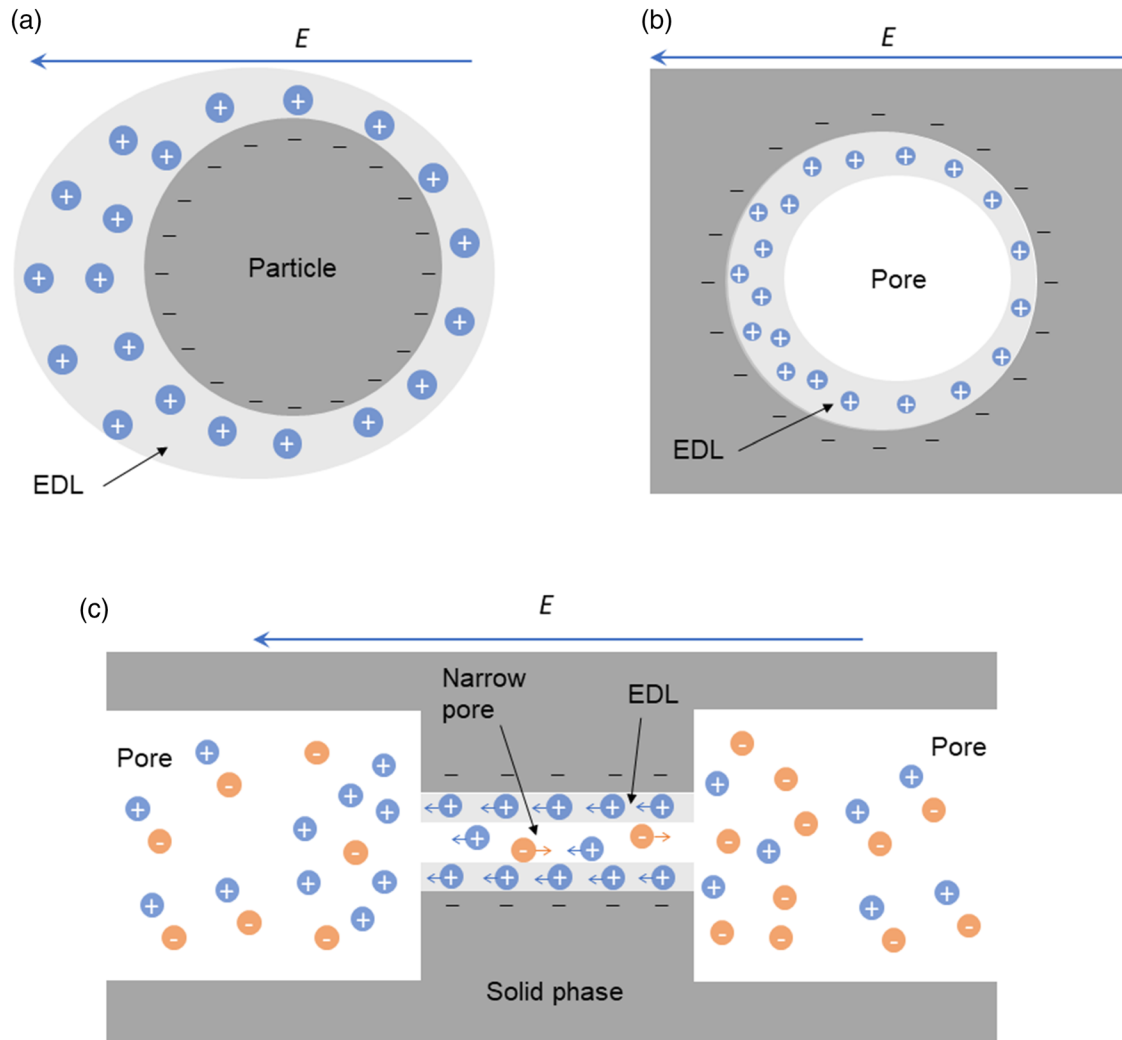
Figure 1. Schematics demonstrating the electrochemical polarizations in water-saturated porous geological media due to the presence of electrical double layer (EDL): (a) grain polarization, (b) pore polarization, and (c) membrane polarization. In the figures, the dark area represents the solid phase, and the gray area represents the EDL. The remaining area is the bulk solution.

Using this concept, many theoretical models have been developed. Assuming that the ions in the EDL can only move tangentially and do not exchange with the bulk solution, Schwarz (1962) developed a Debye type equation to describe the polarization of a spherical grain immersed in electrolyte (Figure 1a). Gains with other shapes were also considered in some studies (e.g., see Dukhin & Shilov, 1980). Note that this type of model is only valid for large grains with $a \gg \lambda$, where λ is the Debye length. A general model is available for grains with arbitrary sizes (e.g., see Chelidze & Gueguen, 1999). In addition to tangential movement, the exchange of ions between the thin EDL and bulk solution (i.e., normal movement) has also been treated, for example, in Fixman (1980).

It is worth addressing that abovementioned models did not distinguish the Stern and diffuse layers. In practice, however, polarization models only considering the tangential ion movement (e.g., Schwarz, 1962) are usually termed *Stern-layer polarization* models (e.g., Jougnot et al., 2010; Revil, 2012). This is because the ions in the EDL of the model do not have normal movement, which is similar to the ions in the Stern layer in a standard EDL model. Similarly, models considering both tangential and normal ion movements are usually termed *diffuse-layer polarization* models (e.g., Lesmes & Morgan, 2001) since the ions in the model are mobile, similar to that in the diffuse layer in the standard EDL model. Recently, many works have been done to combine these two types of models into a generalized EDL polarization model (e.g., Bücker et al., 2019; de Lima & Sharma, 1992; Lesmes & Morgan, 2001; Lyklema et al., 1983; Shilov et al., 2001).

2.3.2. Pore Polarization

The pore polarization model (Figure 1b), which is associated with the pore microstructural model (Figure S1c), assumes that the electrochemical polarization occurs in the pores. For porous rocks, it seems more natural to utilize the pore polarization model rather than the grain model. This is because experimental studies have indicated that the relaxation time of geological materials is controlled by the pore (or pore throat) size rather than the grain size (Revil, Koch, & Holliger, 2012; Scott & Barker, 2003). Few theoretical works have been done to model the polarization occurring in a single pore (Niu & Zhang, 2018b). Theoretical equations developed for grains have been used to model the pore polarization by replacing the grain radius with the pore radius (e.g., see Revil et al., 2015), but no physical justification is provided for such applications.

2.3.3. Membrane Polarization

Consider a sequence of capillary tubes as shown in Figure 1c, in which the wide tubes represent large pore node in porous media while the small tube models a narrow pore throat. Based on this microstructure model, the concept of membrane polarization (Marshall & Madden, 1959) can be adopted, and indeed, it was the earliest conceptual model for induced polarization of porous rocks. The narrow pore throat is treated as a cation-selective zone where the electrical current is mainly carried by cations (i.e., cations have a higher transference number than anions). Under an external electric field, cations will accumulate at one end of the narrow pore throat and deficit at the other side, resulting in an electrically neural concentration gradient (Figure 1c). This concentration gradient imposes an electric dipole moment across the pore throat, and thus, the material is polarized.

Regarding the origin of the cation selectivity of the narrow pore throat in geological media, Bücker and Hördt (2013a) attribute it to the EDL formed at the solid-liquid interface. For pore throats with small sizes (e.g., <0.1 μm), the EDL (usually ~nm in thickness) could occupy a significant volume in the pore throat. Thus, there will be more cations than anions in the pore throat due to the presence of the EDL. After applying an external electric field, the cations will carry more electrical current than anions (e.g., Butt et al., 2013), and thus, the pore throat becomes a cation-selective zone. Analytical equations fully considering the pore geometry and EDL properties have been developed for the polarization of the capillary sequence model (Bücker & Hördt, 2013a). There are also some simplified models by imposing special conditions (e.g., Bücker & Hördt, 2013b).

The abovementioned polarization models (sections 2.3.1 to 2.3.3) have been used to explain the low-frequency permittivity of many materials. For colloidal suspensions in electrolyte solutions (e.g., Arroyo et al., 1999), it is intuitive to apply the grain polarization model (Figure 1a) because the suspended particles can be regarded as discrete grains as shown in Figure S1b. For granular materials such as sands (e.g., Vaudelet et al., 2011) and glass beads packing (e.g., Leroy et al., 2008), it seems still reasonable to apply the grain polarization model (Figure 1a), although the contacting particles in the granular materials are incorrectly treated as isolated grains (Figure S1b). For porous rocks, it is however questionable to model the continuous solid phase with isolated grains and to apply the grain polarization concept. Instead, the concepts of pore polarization and membrane polarization seem more appealing because both of them can be applied to a complex network model (e.g., Figure S1e), which is more realistic for representing the microstructure of porous geological media than the grain model. In addition, recently, the pore polarization concept has gained much attention in estimating the effective pore size of porous rocks with induced polarization measurements (e.g., Revil et al., 2015; Weller et al., 2016).

3. A General Framework for Pore-Scale Modeling

In this section, we propose a general framework for pore-scale numerical modeling of the effective electrical conductivity and permittivity of porous geological materials (Figure 2). In particular, both electrochemical polarizations and interfacial polarization are considered in the framework. To reduce the computational burden, electrochemical polarizations are not modeled from first principle simulations. Instead, the induced complex conductance is calculated at the pore scale using the pore polarization (e.g., Figure 1b) and membrane polarization (e.g., Figure 1c) models with the microstructure of the material simplified as a network of capillary tubes connecting at spherical pore nodes (e.g., Figure S1e). The electrochemical polarizations-induced conductance is then upscaled to the water phase, and the governing equation for the electrical

Determine relevant geometric properties

> **Input:** binary images representing the material microstructure
>
> **Output:** geometric properties such as porosity, surface area, pore size distribution, and pore throat size/length distribution

Calculate electrochemical polarization-induced complex conductance

> **Input:** surface electrochemical properties (e.g., surface charge density and ion mobility) and geometric properties (e.g., pore size distribution and pore throat length distribution)
>
> **Output:** frequency-dependent complex conductance (in S)

Upscale electrochemical polarizations

> **Input:** dynamic pore size and electrochemical polarizations-induced complex conductance
>
> **Output:** an equivalent volumetric complex conductivity (in S m^{-1}) for the fluid phase

Pore-scale numerical simulation of the effective properties

> **Input:** Digital images of the material microstructure and apparent electrical properties of the solid and liquid phases
>
> **Output:** broadband electrical conductivity and permittivity

Figure 2. The framework for pore-scale numerical simulation of the broadband effective electrical conductivity and permittivity of porous rocks used in this study.

conduction is solved in a representative elementary volume (REV) of the material. The REV contains the real microstructure of the material so that the interfacial polarization can be reliably accounted for in the simulation. The proposed framework is outlined in Figure 2, and the details are discussed as follows.

3.1. Determine Relevant Geometric Properties

The first step in the framework is to determine relevant geometric properties of the materials by analyzing the binary microstructural images. The properties of interest include porosity, surface area, pore (node) size distribution, and pore throat size and/or length distribution. One of the purposes of this step is to validate the image processing methods (e.g., noise reduction, smoothing, and segmentation; Andrä et al., 2013a) by comparing the calculated and experimental geometric properties. In addition, some geometric properties such as pore size and pore throat length are critical in modeling the electrochemical polarizations in porous media, and thus, these properties have to be determined for subsequent calculations.

While the bulk properties (e.g., porosity and surface area) are relatively easy to calculate (Zhan et al., 2010), the determination of statistical properties such as pore/grain size distribution and pore throat size (or length) distribution are not straightforward. In this study, we use the pore network extraction algorithms (e.g., Dong & Blunt, 2009; Lindquist et al., 1996; Yi et al., 2017) to determine these properties. Experimental data such as mercury injection porosimetry or gas adsorption data can also be used to estimate these statistical properties, but additional assumptions may be involved, which may not be valid for materials with complex microstructures (e.g., Wardlaw & McKellar, 1981).

3.2. Calculate Electrochemical Polarization-Induced Complex Conductance

The output of most electrochemical polarization models is a complex conductance $C^* = C' - iC''$ (in S; e.g., Schwarz, 1962), and it is only a perturbation caused by the polarization. If no polarization occurs, both the real part C' and imaginary part C'' of the complex conductance are zero. The imaginary part C'' measures the polarizability of the material. The real part C' is related to the displacement current resulting from the

polarization and vanishes if the frequency approaches to zero (i.e., dc condition). Thus, C' should not be confused with the surface conduction, which is induced by migration of excess ions in the EDL of the material even at dc conditions.

As discussed, the pore space of the material is assumed as a network of capillary tubes (narrow pore throat) connecting at some pore nodes (large pores). The elementary pore polarization model (Figure 1b) can be applied to determine the polarization-induced complex conductance C_P^* (r) of individual pores (r being the pore size). The individual contributions C_P^* (r) can then be convolved with the pore size distribution $f(r)$ to calculate the overall response C_P^*, expressed as (e.g., see Leroy et al., 2008; Lesmes & Morgan, 2001)

$$C_P^* = f(r) \otimes C_p^*(r), \tag{9}$$

where $\otimes$ is the convolution product. Similarly, the elementary membrane polarization model (Figure 1c) can be applied to determine the polarization-induced complex conductance $C_m^*(L)$ of individual pore throats (L being a characteristic length of the pore throat). The individual contributions C_m^* (L) can then be convolved with the distribution of the length, that is, $f(L)$, to determine the overall response C_M^*, that is,

$$C_M^* = f(L) \otimes C_m^*(L). \tag{10}$$

The superposition of these two contributions gives a dispersed complex conductance C^* for the electrochemical polarizations of the porous medium,

$$C^* = C_P^* + C_M^*. \tag{11}$$

3.3. Upscale Electrochemical Polarizations

In the models of pore and membrane polarizations, the induced dipole moments are within a pore node or across a pore throat (Figures 1b and 1c). To include them in a pore-scale simulation, we suggest to upscale the electrochemical polarizations by converting the associated complex conductance, C^* (in S), to a complex conductivity $\Delta\sigma_w^*$ (in S m^{-1}), which will be added on the water phase. That is, the water phase will gain an extra complex conductivity in addition to its intrinsic values. The conversion is expressed as (Niu & Zhang, 2017)

$$\Delta\sigma_w^* = \frac{2C^*}{\Lambda}, \tag{12}$$

where Λ is the dynamic pore size proposed in Johnson et al. (1986). For pore space with some simple geometries, the dynamic pore size Λ can be analytically determined. For example, if all the pores in the materials are spherical and identical, Λ is then equal to the radius of the pores. For complex microstructures, however, Λ needs to be numerically determined based on the definition (Johnson et al., 1986),

$$\frac{2}{\Lambda} = \frac{\int |\mathbf{E}(\mathbf{x})|^2 dV}{\int |\mathbf{E}(\mathbf{x})|^2 dS}, \tag{13}$$

where $\mathbf{E}(\mathbf{x})$ is the local electric field at location $\mathbf{x}$, dV denotes the integration that is over the pore space, and dS indicates the integration that is over the solid-liquid interface. To calculate Λ, the local electric field $\mathbf{E}(\mathbf{x})$ needs to be determined by solving the Laplace equation.

In modeling the effective electrical properties of colloidal suspension and geological materials, it is very common to convert the surface electrochemical processes-induced conductance (in S) to a volumetric conductivity (in S m^{-1}). In general, there are two ways to upscale the surface conductance: particle upscaling and pore upscaling (Niu & Zhang, 2017). The particle upscaling has been long used in modeling the low-frequency electrical properties of colloidal suspension (e.g., O'Konski, 1960; Schwarz, 1962), for which the grain polarization can be safely applied because the induced dipole moment is across the particles. However, for porous geological materials, the dipole moment induced by electrochemical polarizations is within pore nodes or across pore throats, and hence, it is logical to use the pore upscaling, that is, Equation 12.
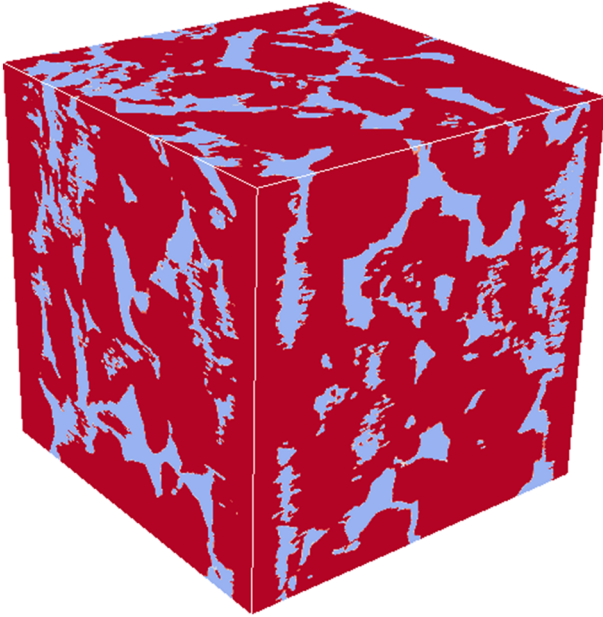
Figure 3. A binary image of the Berea sandstone sample (350^3 voxels) obtained from μCT scan images after segmentation. The size of each voxel is 2.8 × 2.8 × 2.8 μm.

3.4. Pore-Scale Numerical Simulation of the Effective Properties

Nonmetallic minerals are usually nonconductive, and thus, the complex conductivity of the solid phase only has an imaginary component, that is, $i\omega\varepsilon_s$, where ε_s is the high-frequency permittivity (or dielectric permittivity) of the solid phase. The complex conductivity of the water has both real and imaginary components. While the real component is water conductivity σ_w, the imaginary component is $i\omega\varepsilon_w$, where ε_w is the high-frequency permittivity (or dielectric permittivity) of water. After upscaling the electrochemical polarizations, the water phase now has an apparent complex conductivity σ_w^*,

$$\sigma_w^* = \sigma_w + i\omega\varepsilon_w + \Delta\sigma_w^*. \tag{14}$$

The pore-scale numerical simulation of the effective complex conductivity can be conducted by solving the Laplace equation in a REV of the sample,

$$\nabla \cdot \mathbf{J}_t = -\nabla \cdot \left[\sigma_\mathbf{x}^* \nabla u\right] = 0, \tag{15}$$

where $\sigma_\mathbf{x}^*$ is the complex conductivity at the spatial location $\mathbf{x}$ within the material and u is the electrical potential at $\mathbf{x}$. If $\mathbf{x}$ is located within the solid phase, $\sigma_\mathbf{x}^* = i\omega\varepsilon_s$; otherwise, $\sigma_\mathbf{x}^* = \sigma_w^*$. In the simulation, an electrical potential gradient is applied across the REV, and the spatial distributions of u and $\mathbf{J}_t$ are determined numerically. The associated local electric field $\mathbf{E}$ can also be determined accordingly. Then, the effective complex conductivity of the sample σ_{eff}^* can be determined as (Torquato, 2013)

$$\sigma_{eff}^* = \frac{<\mathbf{J}_t>}{<\mathbf{E}>}, \tag{16}$$

where $<\mathbf{E}>$ and $<\mathbf{J}_t>$ are the volume-averaged electric field and current density of the material, respectively.

4. Application to Berea Sandstone

In this study, we select a Berea sandstone sample to demonstrate the use of the proposed framework. Experiments were also conducted to measure the effective electrical conductivity and permittivity of the sample in the frequency range between 10^{-3} and 10^9 Hz. The details of the experiment and simulation are introduced in this section.

4.1. Sample and Experiment

The porosity ϕ of the Berea sandstone sample is 20.2%, and the specific surface area S_m is 0.5 m^2 g^{-1} as determined by nitrogen adsorption. Previous studies showed that the Berea sandstone is mainly made of quartz with a minor amount, less than 4% of clay minerals (e.g., Knight & Nur, 1987). The microstructure of the sample is shown in Figure 3 with a resolution of 2.8 μm, which are resampled from the μCT scan images of the sample after segmentation. The intrinsic formation factor F of the sample is 16.3 as determined by multisalinity electrical measurements (Revil et al., 2016).

To determine the statistical properties of the microstructure, the pore space of the Berea sample is assumed as a lattice of pores connected by throats. Here, we use the algorithm developed by Dong and Blunt (2009) to extract the geometric characteristics from the binary images. The results include the pore size distribution (Figure 4a) and pore throat length distribution (Figure 4b). These statistical properties will be used later to calculate the complex conductance induced by electrochemical polarizations.

The electrical properties of the sample, which was saturated by NaCl solution with $\sigma_w = 0.043$ S m^{-1}, were measured with two different instruments. For frequencies lower than 10 kHz, the complex conductivity was measured by an impedance meter (PSIP, Ontash & Ermac, Inc., USA) with the four-terminal method and Ag-AgCl nonpolarizable electrodes. For the frequency ranging between 1 MHz and 1 GHz, the complex
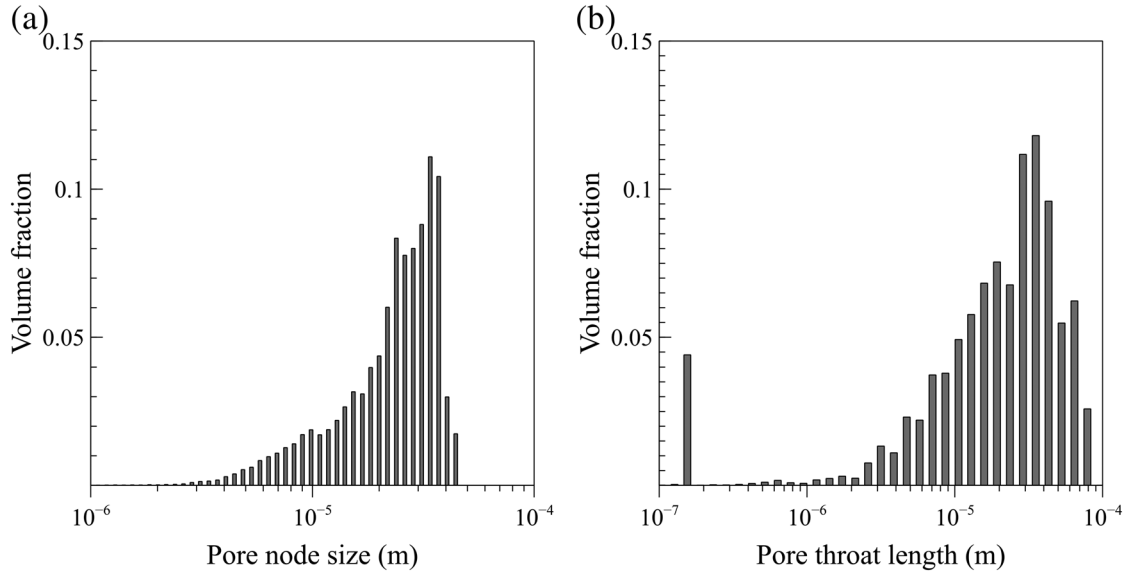
Figure 4. The geometric properties of the Berea sandstone sample: (a) pore node size distribution and (b) pore throat length distribution.

permittivity was measured with a coaxial probe (N1501A-101, Keysight, Inc., USA) and a network analyzer (E5071C, Keysight, Inc., USA). The experimental results are shown in Figure 5.

4.2. Pore-Scale Numerical Simulation

The effective complex conductivity of the sample was also calculated by solving Equations 15 and 16. In the calculation, the binary microstructural images in Figure 3 were used, and the considered frequency range is between 10^{-3} and 10^9 Hz. The electrical conductivity and dielectric permittivity of the pore water is 0.043 S m^{-1} and $80\varepsilon_0$ (ε_0 being the vacuum permittivity 8.85×10^{-12} F m^{-1}), respectively; the solid phase is nonconductive, and the dielectric permittivity is $7\varepsilon_0$. Both the pore polarization and membrane polarization are considered in the calculation. For the pore polarization, Schwarz's (1962) model is used to calculate the polarization-induced complex electrical conductance C_P^*, expressed as

$$C_p^* = \frac{i\omega\tau_p}{1 + i\omega\tau_p}\Sigma_S,$$ (17)

where Σ_S (in S) is the surface conductance related to the EDL, and the relaxation time constant τ_p is expressed as

$$\tau_p = \frac{r^2}{2D},$$ (18)

where D (in m^2 s^{-1}) is the diffusion coefficient of the counterions in the EDL and r is the pore radius. Note that Equations 17 and 18 are modified from Schwarz (1962) by replacing the particle size a with the pore size r. In our simulation, Σ_S is 1.3×10^{-9} S, which corresponds to a typical surface charge density of silica (0.025 C m^{-2}) with Na$^+$ mobility of 5.19×10^{-8} m^2 V^{-1} s^{-1}. The pore size distribution in Figure 4a is used to account for the contributions from all the pores (Equation 9).

For membrane polarization, we use Titov's narrow pore throat model (Titov et al., 2002) to calculate the polarization-induced complex conductance. The output of Titov's membrane polarization model is the complex resistance Z_m^* of the pore throat, expressed as (e.g., Bücker & Hördt, 2013b)

$$Z_m^* = Z_{dc}\left[1 - \eta_0\left(1 - \frac{1 - \exp\left(-2\sqrt{i\omega\tau_m}\right)}{2\sqrt{i\omega\tau_m}}\right)\right],$$ (19)

where Z_{dc} is the dc resistance of the pore throat, η_0 is the polarizability of the material, and the relaxation time constant τ_m is related to the pore throat length L by
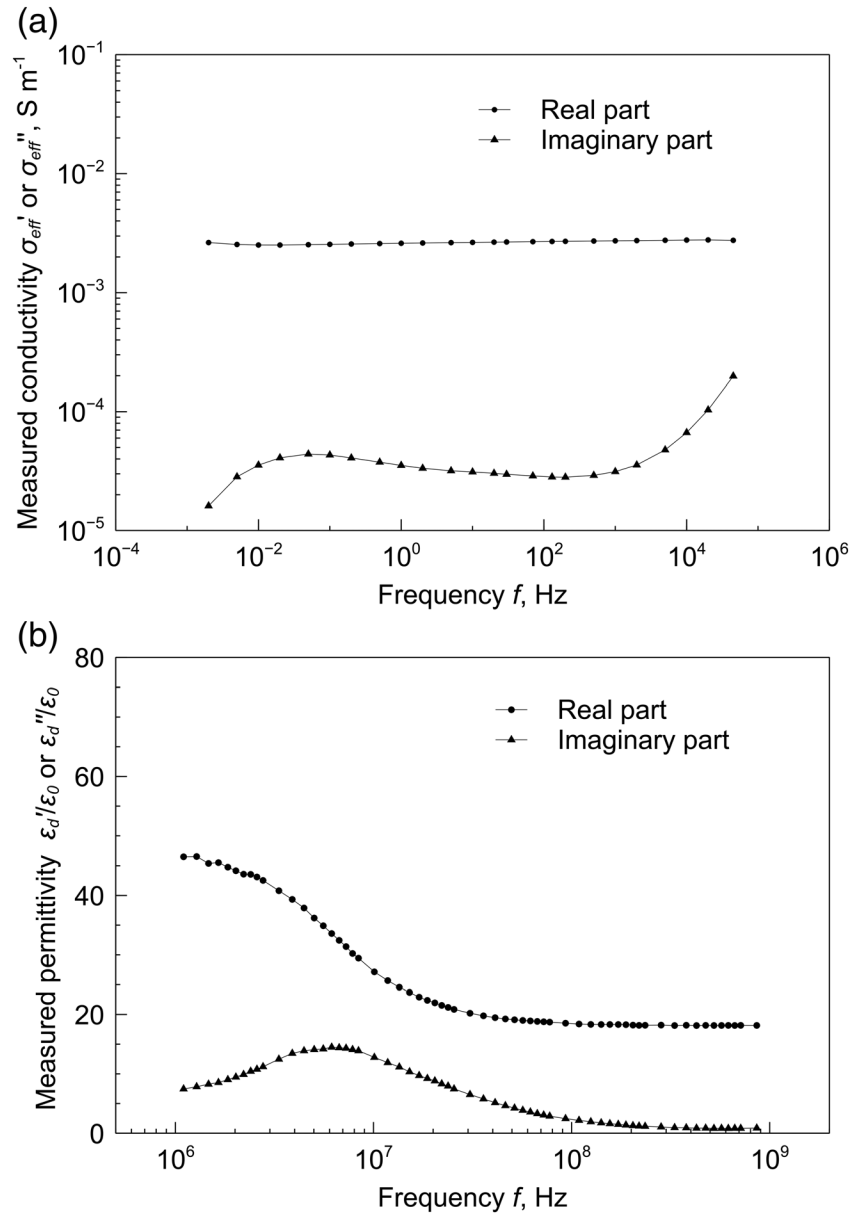
Figure 5. Measured electrical properties of the Berea sandstone sample: (a) complex effective conductivity measured by an impedance meter with four-terminal method and Ag-AgCl electrodes and (b) effective complex permittivity ε_d^* measured with the coaxial probe and a network analyzer (ε_0 being the vacuum permittivity).

$$\tau_m = \frac{L^2}{4D}. \tag{20}$$

For 1-D system (e.g., Marshall & Madden, 1959), the unit of Z_m^* is Ωm^2; for 3-D system shown in Figure 1c, the unit of Z_m^* is Ω (Bücker & Hördt, 2013b). Note that the complex conductance of the pore throat (i.e., $1/Z_m^*$) also contains the dc component of the conductance of the pore throat $1/Z_{dc}$, which is not influenced by the membrane polarization. To determine the membrane polarization-induced complex conductance perturbation C_m^*, this dc component needs to be subtracted, and thus, we have

$$C_m^* = 1/Z_m^* - 1/Z_{dc}. \tag{21}$$

Table 1
Summary of Petrophysical Properties of the Berea Sandstone Sample and Parameters Used in the Pore-Scale Numerical Simulation

Petrophysical properties	
Porosity (ϕ)	20.2%
Specific surface area (S_m)	0.5 m^2 g^{-1}
Formation factor (F)	16.3[a]
Mean pore size (r_m)	35 µm
Parameters used in the simulation	
Surface conductance contributing to the pore polarization (Σ_S)	1.3×10^{-9} S
Water conductivity (σ_w)	0.043 S m^{-1}
Diffusion coefficient of Na$^+$ in EDL (D)	1.3×10^{-9} m^2 s^{-1}
Dynamic pore size (Λ)	2.7 µm
Polarizability in modeling the membrane polarization (η_0)	1%
Intrinsic permittivity of the solid phase (ε_s)	$7\varepsilon_0$
Intrinsic permittivity of water (ε_w)	$80\varepsilon_0$

Note. The electrical permittivity of vacuum ε_0 is 8.85×10^{-12} F m^{-1}.
[a]From Revil et al. (2016).

In our calculation, Z_{dc} of the pore throat is calculated by considering the pore throat geometry (size and length) and the pore water conductivity. The polarizability η_0 used in the calculation is 1%, which is close to the value (~0.6%) reported in Lesmes and Frye (2001). For each pore throat, the relaxation time τ_m is calculated with Equation 21. Similarly, the contributions of all pore throats are determined using Equation 10 by considering the pore throat length distribution in Figure 4b. In the calculation, the diffusion coefficient of the counterion D was 1.3×10^{-9} m^2 s^{-1}, which is consistent with the Na$^+$ mobility 5.19×10^{-8} m^2 V^{-1} s^{-1} if consider the Nernst-Einstein equation.

The calculated complex conductance of pore and membrane polarizations is superpositioned to form the electrochemical polarizations-induced conductance C^* (Equation 11). Then, the conductance C^* is converted to a volumetric electrical conductivity for the water phase, that is, Equation 12. The dynamic pore size of the sample is 2.7 µm as determined from Equation 13. In this study, an industrial standard code (AC3D.F) developed at National Institute of Standards and Technology was modified to conduct the simulation. The code uses the finite-difference method to solve the governing equation (Equation 15), and a total of 350^3 voxels with the same size was used to approximate the REV in Figure 3. Table 1 summarizes the basic properties of the rock sample and parameters used in the numerical simulation. We emphasize that the electrochemical polarization models used in the calculation are only for demonstration purpose. Other polarization models may also be used.

5. Comparison of Experimental and Numerical Results

5.1. Effective Electrical Conductivity

The simulated and measured effective conductivity spectra of the sample are shown in Figure 6. For frequencies lower than 10^5 Hz, the measured effective conductivity is directly from the four-terminal method (Figure 5a). In the frequency range between 1 MHz and 1 GHz, the effective conductivity measurements presented in Figure 6 are calculated from the measured effective imaginary permittivity ε''_d in Figure 5b. In
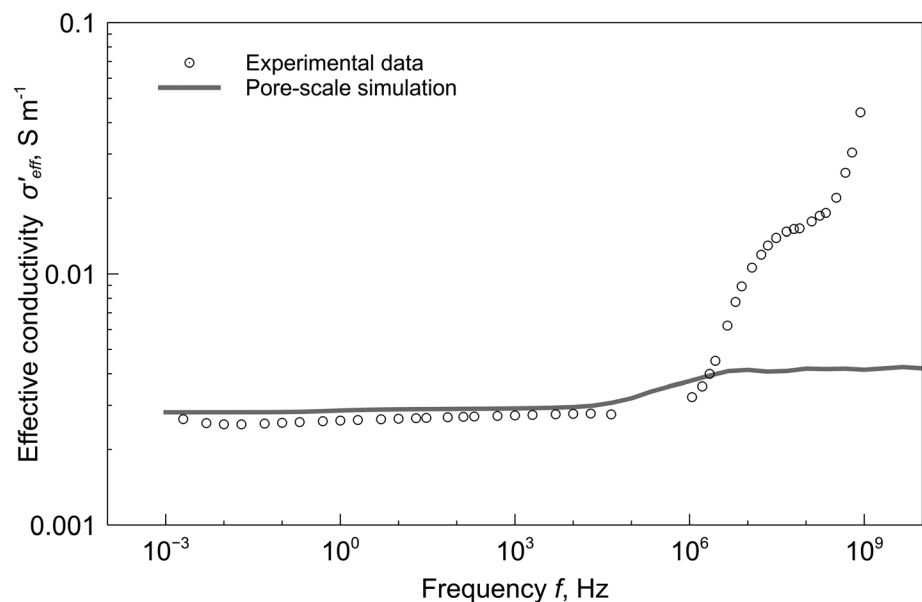

Figure 6. The simulated and measured effective conductivity σ'_{eff} of the Berea sandstone sample in the frequency range between 10^{-3} and 10^9 Hz.

addition, because ε''_d only accounts for the relaxation losses, a dc conductivity σ_{dc} is also added, and thus, the effective conductivity σ'_{eff} is equal to $\sigma_{dc} + \omega\varepsilon''_d$ (see Equation 7 and Topp et al., 1988). In this study, σ_{dc} is equal to 0.0278 S m^{-1} as determined as the lowest measured effective real conductivity (Figure 5a).

A comparison of numerical and experimental results shows that the simulation captures the general trend of the effective conductivity variations, especially for frequencies lower than 1 MHz. When the frequency is larger than 1 MHz, both simulated and measured values increase due to the interfacial polarization (will be discussed in section 5.3). However, the magnitude of the increase in the simulation is only ~0.001 S m^{-1}, which is much smaller than that in the experiment (~0.02 S m^{-1}). This discrepancy might be due to fact that the resolution of the digital microstructural μCT images (e.g., Figure 3) did not capture the nanometer-scale heterogeneities at the solid-liquid interface. Since the interfacial polarization is associated with electrical discontinuities, ignoring these nanometer-scale discontinuities in the simulation underestimates the relaxation losses and thus the effective electrical conductivity as shown in Figure 6.

5.2. Effective Electrical Permittivity

The simulated and measured effective electrical permittivity ε'_{eff} of the sample is shown in Figure 7a. It is observed that the effective permittivity varies over several orders as the frequency changes. At frequencies between 10^8 and 10^9 Hz, the effective relative permittivity (i.e., ε'_{eff} normalized by ε_0) is nearly constant, ~18 for the experiment and ~12 for the simulation. These effective permittivity values are very close to the volume-averaged permittivity of the individual phases, implying that no polarizations occur in this frequency range. When the frequency is decreased to ~10^6 Hz, the experimental spectrum shows a clear increase in effective permittivity ($\varepsilon'_{eff}/\varepsilon_0$ increased to ~45) due to the interfacial polarization (will be discussed in section 5.3). However, the increase in effective permittivity was not observed in numerical results. As the frequency is further decreased (<10^5 Hz), the simulated and measured spectra agree well, and both of them increase sharply due to the electrochemical polarizations (will be discussed in section 5.3). When the frequency is lower than 0.1 Hz, large discrepancies are observed between experimental data and numerical results.

The corresponding effective imaginary conductivity spectra are also plotted in Figure 7b. Note that the effective real permittivity ε'_{eff} and effective imaginary conductivity σ''_{eff} are related to each other by $\sigma''_{eff} = \omega\varepsilon'_{eff}$. In a $\sigma''_{eff} - f$ log-log plot, a constant permittivity is shown as a straight line with a slope of ω; an increase in the permittivity is exhibited as a shift of the straight line toward the low-frequency side. Our discussions on the effective permittivity in Figure 7a also hold for the effective imaginary conductivity in Figure 7b.

5.3. Individual Contributions

To identify the relative contribution of individual polarizations, we also conducted simulations that only consider one polarization at a time. In simulating the interfacial polarization, only the high-frequency permittivity (or dielectric permittivity) and dc conductivity are assigned to the solid and water phases. In simulating the pore or membrane polarization, the complex conductivity of the water phase is $\sigma_w + \Delta\sigma^*_w$, in which $\Delta\sigma^*_w$ is converted from either C^*_P (pore polarization) or C^*_M (membrane polarization); the complex conductivity of the solid phase is set as zero. Other parameters used in the simulations are identical to that in Table 1. The calculated relative contributions of individual polarizations to the effective permittivity of the sample are also shown in Figure 7.

The simulated effective permittivity due to the interfacial polarization (blue line in Figure 7a) is similar to the experiment results, and both curves exhibit a high permittivity plateau ($\varepsilon'_{eff}/\varepsilon_0 = $ ~40) at low frequencies (<10^5 Hz) and a low effective permittivity ($\varepsilon'_{eff}/\varepsilon_0 = $ ~20) at high frequencies (>10^8 Hz). The characteristic frequency where the effective permittivity experiences a sharp change is, however, different, ~5×10^5 Hz for the simulation and ~10^7 Hz for the experiment. One possible explanation of this discrepancy is that the binary images used in the simulation have smoother solid-liquid interfaces than the real sample, and thus, interfacial polarizations associated with fine-scale heterogeneity could be overlooked in the simulation. Thus, the characteristic frequency of the simulated spectrum shifts to the low-frequency side as shown in Figure 7.

The membrane polarization (red line in Figure 7) seems to affect the effective permittivity in a broad frequency range, dominating around 10^3 Hz. If the membrane polarization is not accounted for, the
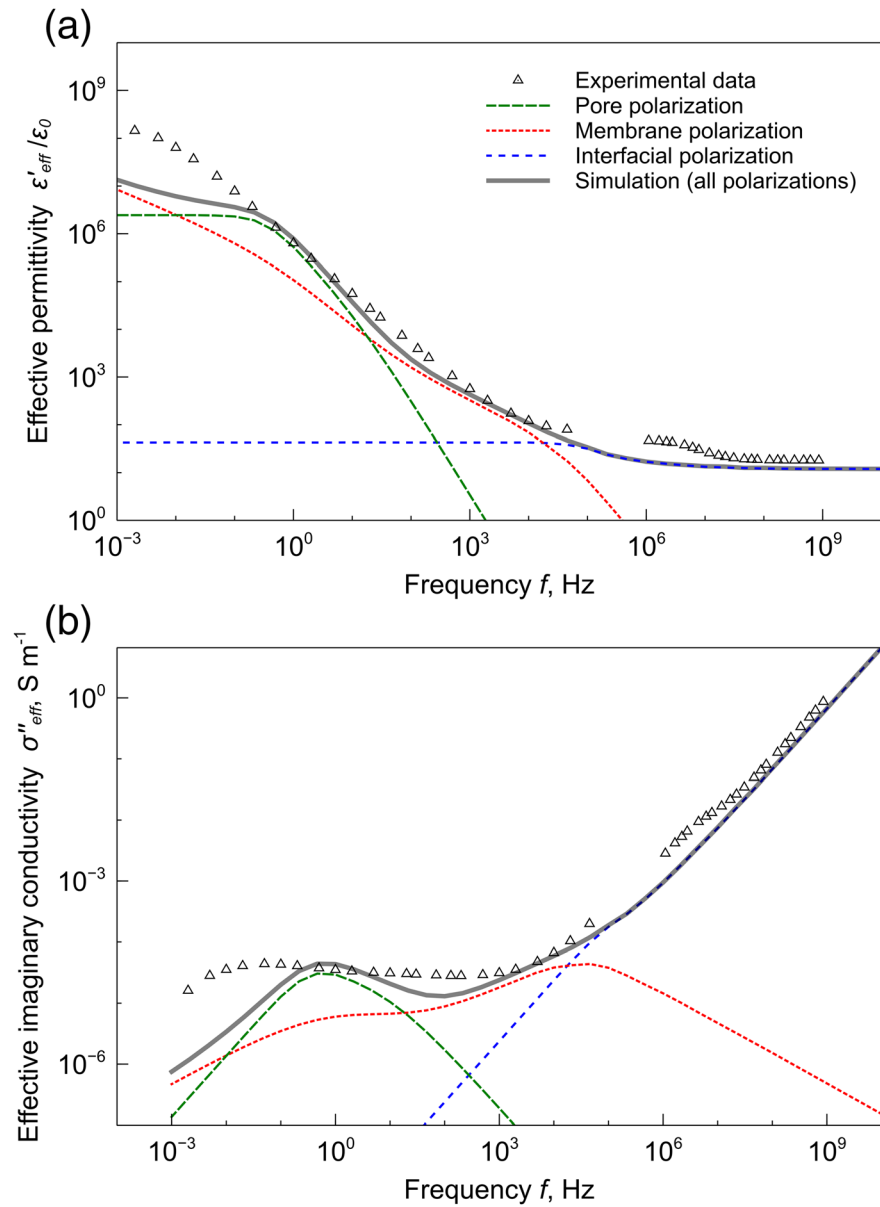
Figure 7. The simulated and measured (a) effective real permittivity and (b) effective imaginary conductivity of the Berea sandstone sample in the frequency range between 10^{-3} and 10^9 Hz.

superposition of pore and interfacial polarization will significantly underestimate the effective permittivity at intermediate frequencies (e.g., from ~10 to ~10^4 Hz). The underestimation has been demonstrated in some previous studies that did not consider the membrane polarization (e.g., Lesmes & Morgan, 2001). In Figure 7, the simulated effective permittivity considering all polarizations agrees well at the intermediate frequencies with the experimental curve. This implies that the membrane polarization could be a significant contributor to the effective permittivity of porous geological materials (e.g., Bücker & Hördt, 2013b).

At low frequencies (<10^2 Hz), it appears that the pore polarization (green line in Figure 7) dominates over other polarizations, and the effective permittivity increase is significant. Comparing to experimental data, the frequency range affected by the pore polarization is much narrower in the simulation. For frequencies lower than 0.1 Hz, the simulated effective permittivity is considerably low. This could be because the

binary images used in the simulation only cover a small fraction of the sample (~1 mm^3), and polarizations occurring in larger pores may not be accounted for in the simulation.

5.4. Potential Applications

The proposed framework can be used to improve our understanding and modeling of the broadband effective electrical conductivity and permittivity of porous geological materials, which are essential in interpreting field geoelectrical measurements. In particular, the proposed framework is well suited for studying the variation in effective electrical properties induced by various electrochemical processes occurring at the pore or subpore scale. Also, because different models of electrochemical polarizations can be easily incorporated in the simulation, it can be used to evaluate the effectiveness of existing models. One example is to compare the individual contributions of the Stern-layer polarization and diffuse-layer polarization (e.g., Bücker et al., 2019) in samples with realistic microstructures.

Another application of the proposed framework is to study the role of material microstructure in controlling the effective electrical properties of geological materials. Recently, it becomes possible for pore-scale numerical simulations to include various geological processes, for example, compaction (Niu & Zhang, 2018a) and mineral precipitation and dissolution (e.g., Miller et al., 2017; Niu & Zhang, 2019). Thus, realistic microstructure resulted from these geological processes can be effectively generated from numerical experiments. Coupled with the proposed framework, the geoelectrical signatures of these geological processes can be quantified and linked to the microstructural changes. In this regard, our work becomes an attractive way to develop geological process-based electrical models for porous media.

6. Conclusions

In this study, we developed a general framework for pore-scale numerical simulations of the effective electrical conductivity and permittivity of porous media in a broad frequency range. Both electrochemical polarizations and interfacial polarization are considered in our framework. To account for electrochemical polarizations, the pore space of geological materials is assumed as a lattice of pore nodes connected by pore throats. Then, the concepts of pore polarization and membrane polarization are respectively applied to the pore nodes and pore throats so that the effects of electrochemical processes in the entire pore space can be quantified. The electrochemical polarization-induced complex conductance is then upscaled to the water phase, which gains an extra volumetric complex conductivity in addition to its intrinsic value. The pore-scale numerical simulation can then be conducted on the digital microstructure of the material using the apparent material properties. By doing so, both interfacial polarization (resulted from electrical discontinuities) and electrochemical polarizations (due to the presence of the EDL) can be considered in a pore-scale simulation.

A Berea sandstone sample is utilized to demonstrate the use of the framework. A comparison of numerical and experimental results shows that effective electrical conductivity and permittivity spectra in general agree very well in the frequency between 10^{-3} and 10^9 Hz. At high frequencies (>10^5 Hz) where the interfacial polarization dominates, both simulation and experiment show a clear increase in the effective permittivity as the frequency decreases. However, the characteristic frequency, at which the effective permittivity experiences a significant change, is much lower in the simulation than that in the experiment. This discrepancy can be explained by the fact that the microstructural images used in the simulation have smoother solid-liquid interfaces than the real sample. Thus, interfacial polarizations associated with fine-scale heterogeneity could be overlooked in the simulation.

At intermediate frequencies (e.g., from 10^2 to 10^5 Hz), the membrane polarization has a significant contribution to the effective permittivity of the material. If overlooked, the simulated effective permittivity will be much smaller than the measured values. For frequencies lower than 100 Hz, the pore polarization dominates over other polarizations. It seems that the frequency range affected by the pore polarization in the simulation is much narrower than that in the experiment. In particular, the simulated low-frequency effective permittivity (<0.1 Hz) is systemically low. This may be due to the use of a small sample volume (~1 mm^3) in the simulation that cannot consider the polarizations occurring in larger pores.

Data Availability Statement

The data presented in this study can be downloaded online (http://doi.org/10.5281/zenodo.3908737).

References

Andrä, H., Combaret, N., Dvorkin, J., Glatt, E., Han, J., Kabel, M., et al. (2013a). Digital rock physics benchmarks—Part I: Imaging and segmentation. *Computers & Geosciences*, *50*, 25–32. https://doi.org/10.1016/j.cageo.2012.09.005

Andrä, H., Combaret, N., Dvorkin, J., Glatt, E., Han, J., Kabel, M., et al. (2013b). Digital rock physics benchmarks—Part II: Computing effective properties. *Computers & Geosciences*, *50*, 33–43. https://doi.org/10.1016/j.cageo.2012.09.008

Annan, A. P. (2005). Ground-penetrating radar. In *Near-surface geophysics* (pp. 357–438). Tulsa, OK: Society of Exploration Geophysicists.

Archie, G. E. (1942). The electrical resistivity log as an aid in determining some reservoir characteristics. *Transactions of AIME*, *146*(01), 54–62. https://doi.org/10.2118/942054-G

Arroyo, F. J., Carrique, F., Bellini, T., & Delgado, A. V. (1999). Dielectric dispersion of colloidal suspensions in the presence of Stern layer conductance: Particle size effects. *Journal of Colloid and Interface Science*, *210*(1), 194–199. https://doi.org/10.1006/jcis.1998.5914

Bairlein, K., Bücker, M., Hördt, A., & Hinze, B. (2016). Temperature dependence of spectral induced polarization data: Experimental results and membrane polarization theory. *Geophysical Journal International*, *205*(1), 440–453. https://doi.org/10.1093/gji/ggw027

Blunt, M. J., Bijeljic, B., Dong, H., Gharbi, O., Iglauer, S., Mostaghimi, P., et al. (2013). Pore-scale imaging and modelling. *Advances in Water Resources*, *51*, 197–216. https://doi.org/10.1016/j.advwatres.2012.03.003

Bücker, M., Flores Orozco, A., Undorf, S., & Kemna, A. (2019). On the role of Stern- and diffuse-layer polarization mechanisms in porous media. *Journal of Geophysical Research: Solid Earth*, *124*, 5656–5677. https://doi.org/10.1029/2019JB017679

Bücker, M., & Hördt, A. (2013a). Analytical modelling of membrane polarization with explicit parametrization of pore radii and the electrical double layer. *Geophysical Journal International*, *194*(2), 804–813. https://doi.org/10.1093/gji/ggt136

Bücker, M., & Hördt, A. (2013b). Long and short narrow pore models for membrane polarization. *Geophysics*, *78*(6), E299–E314. https://doi.org/10.1190/geo2012-0548.1

Bussian, A. E. (1983). Electrical conductance in a porous medium. *Geophysics*, *48*(9), 1258–1268. https://doi.org/10.1190/1.1441549

Butt, H. J., Graf, K., & Kappl, M. (2013). *Physics and chemistry of interfaces*. Hoboken, NJ: John Wiley & Sons.

Chelidze, T. L., & Gueguen, Y. (1999). Electrical spectroscopy of porous rocks: A review—I. Theoretical models. *Geophysical Journal International*, *137*(1), 1–15. https://doi.org/10.1046/j.1365-246x.1999.00799.x

Chen, Y., & Or, D. (2006). Geometrical factors and interfacial processes affecting complex dielectric permittivity of partially saturated porous media. *Water Resources Research*, *42*, W06423. https://doi.org/10.1029/2005WR004744

Constable, S. (2010). Ten years of marine CSEM for hydrocarbon exploration. *Geophysics*, *75*(5), 75A67–75A81. https://doi.org/10.1190/1.3483451

Cosenza, P., Ghorbani, A., Revil, A., Zamora, M., Schmutz, M., Jougnot, D., & Florsch, N. (2008). A physical model of the low-frequency electrical polarization of clay rocks. *Journal of Geophysical Research*, *113*, B08204. https://doi.org/10.1029/2007JB005539

Cundall, P. A., & Strack, O. D. (1979). A discrete numerical model for granular assemblies. *Geotechnique*, *29*(1), 47–65. https://doi.org/10.1680/geot.1979.29.1.47

de Lima, O. A., & Sharma, M. M. (1992). A generalized Maxwell-Wagner theory for membrane polarization in shaly sands. *Geophysics*, *57*(3), 431–440. https://doi.org/10.1190/1.1443257

Dong, H., & Blunt, M. J. (2009). Pore-network extraction from micro-computerized-tomography images. *Physical Review E*, *80*(3), 036307.

Dukhin, S. S., & Shilov, V. N. (1980). Kinetic aspects of electrochemistry of disperse systems. Part II. Induced dipole moment and the non-equilibrium double layer of a colloid particle. *Advances in Colloid and Interface Science*, *13*(1–2), 153–195.

Fixman, M. (1980). Charged macromolecules in external fields. I. The sphere. *The Journal of Chemical Physics*, *72*(9), 5177–5186. https://doi.org/10.1063/1.439753

Han, T., & Yang, Y. S. (2018). Numerical and theoretical simulations of the dielectric properties of porous rocks. *Journal of Applied Geophysics*, *159*, 186–192. https://doi.org/10.1016/j.jappgeo.2018.08.014

Hanai, T. (1960). Theory of the dielectric dispersion due to the interfacial polarization and its application to emulsions. *Kolloid Zeitschrift*, *171*(1), 23–31. https://doi.org/10.1007/BF01520320

Hartkamp, R., Biance, A. L., Fu, L., Dufrêche, J. F., Bonhomme, O., & Joly, L. (2018). Measuring surface charge: Why experimental characterization and molecular modeling should be coupled. *Current Opinion in Colloid & Interface Science*, *37*, 101–114. https://doi.org/10.1016/j.cocis.2018.08.001

Johnson, D. L., Koplik, J., & Schwartz, L. M. (1986). New pore-size parameter characterizing transport in porous media. *Physical Review Letters*, *57*(20), 2564.

Jones, S. B., & Friedman, S. P. (2000). Particle shape effects on the effective permittivity of anisotropic or isotropic media consisting of aligned or randomly oriented ellipsoidal particles. *Water Resources Research*, *36*(10), 2821–2833. https://doi.org/10.1029/2000WR900198

Jougnot, D., Ghorbani, A., Revil, A., Leroy, P., & Cosenza, P. (2010). Spectral induced polarization of partially saturated clay-rocks: A mechanistic approach. *Geophysical Journal International*, *180*(1), 210–224. https://doi.org/10.1111/j.1365-246X.2009.04426.x

Kemna, A., Binley, A., Cassiani, G., Niederleithinger, E., Revil, A., Slater, L., et al. (2012). An overview of the spectral induced polarization method for near-surface applications. *Near Surface Geophysics*, *10*(6), 453–468. https://doi.org/10.3997/1873-0604.2012027

Kneisel, C., Hauck, C., Fortier, R., & Moorman, B. (2008). Advances in geophysical methods for permafrost investigations. *Permafrost and Periglacial Processes*, *19*(2), 157–178. https://doi.org/10.1002/ppp.616

Knight, R. (2001). Ground penetrating radar for environmental applications. *Annual Review of Earth and Planetary Sciences*, *29*(1), 229–255. https://doi.org/10.1146/annurev.earth.29.1.229

Knight, R. J., & Nur, A. (1987). The dielectric constant of sandstones, 60 kHz to 4 MHz. *Geophysics*, *52*(5), 644–654. https://doi.org/10.1190/1.1442332

Kremer, F., & Schönhals, A. (2002). *Broadband dielectric spectroscopy*. New York: Springer Science & Business Media.

Kuras, O., Beamish, D., Meldrum, P. I., & Ogilvy, R. D. (2006). Fundamentals of the capacitive resistivity technique. *Geophysics*, *71*(3), G135–G152. https://doi.org/10.1190/1.2194892

Leroy, P., Revil, A., Kemna, A., Cosenza, P., & Ghorbani, A. (2008). Complex conductivity of water-saturated packs of glass beads. *Journal of Colloid and Interface Science*, *321*(1), 103–117. https://doi.org/10.1016/j.jcis.2007.12.031

Lesmes, D. P., & Friedman, S. P. (2005). Relationships between the electrical and hydrogeological properties of rocks and soils. In *Hydrogeophysics* (pp. 87–128). Dordrecht: Springer.

Lesmes, D. P., & Frye, K. M. (2001). Influence of pore fluid chemistry on the complex conductivity and induced polarization responses of Berea sandstone. *Journal of Geophysical Research*, *106*(B3), 4079–4090. https://doi.org/10.1029/2000JB900392

Lesmes, D. P., & Morgan, F. D. (2001). Dielectric spectroscopy of sedimentary rocks. *Journal of Geophysical Research*, *106*(B7), 13,329–13,346. https://doi.org/10.1029/2000JB900402

Lindquist, W. B., Lee, S. M., Coker, D. A., Jones, K. W., & Spanne, P. (1996). Medial axis analysis of void structure in three-dimensional tomographic images of porous media. *Journal of Geophysical Research*, *101*(B4), 8297–8310. https://doi.org/10.1029/95JB03039

Loke, M. H., Chambers, J. E., Rucker, D. F., Kuras, O., & Wilkinson, P. B. (2013). Recent developments in the direct-current geoelectrical imaging method. *Journal of Applied Geophysics*, *95*, 135–156. https://doi.org/10.1016/j.jappgeo.2013.02.017

Lyklema, J., Dukhin, S. S., & Shilov, V. N. (1983). The relaxation of the double layer around colloidal particles and the low-frequency dielectric dispersion: Part I. Theoretical considerations. *Journal of Electroanalytical Chemistry and Interfacial Electrochemistry*, *143*(1–2), 1–21. https://doi.org/10.1016/S0022-0728(83)80251-4

Marshall, D. J., & Madden, T. R. (1959). Induced polarization, a study of its causes. *Geophysics*, *24*(4), 790–816. https://doi.org/10.1190/1.1438659

McBride, M. B. (1989). Surface chemistry of soil minerals. In *Minerals in soil environments* (pp. 35–88). Madison, WI: Soil Science Society of America.

Mendelson, K. S., & Cohen, M. H. (1982). The effect of grain anisotropy on the electrical properties of sedimentary rocks. *Geophysics*, *47*(2), 257–263. https://doi.org/10.1190/1.1441332

Miller, K., Vanorio, T., & Keehm, Y. (2017). Evolution of permeability and microstructure of tight carbonates due to numerical simulation of calcite dissolution. *Journal of Geophysical Research: Solid Earth*, *122*, 4460–4474. https://doi.org/10.1002/2017JB013972

Milton, G. W., Eyre, D. J., & Mantese, J. V. (1997). Finite frequency range Kramers-Kronig relations: Bounds on the dispersion. *Physical Review Letters*, *79*(16), 3062.

Niu, Q., Revil, A., Li, Z., & Wang, Y. H. (2017). Relationship between electrical conductivity anisotropy and fabric anisotropy in granular materials during drained triaxial compressive tests: A numerical approach. *Geophysical Journal International*, *210*(1), 1–17. https://doi.org/10.1093/gji/ggx140

Niu, Q., & Zhang, C. (2017). Pore-scale modelling of complex conductivity of saturated granular materials. *Near Surface Geophysics*, *15*(6), 593–602. https://doi.org/10.3997/1873-0604.2017055

Niu, Q., & Zhang, C. (2018a). Physical explanation of Archie's porosity exponent in granular materials: A process-based, pore-scale numerical study. *Geophysical Research Letters*, *45*, 1870–1877. https://doi.org/10.1002/2017GL076751

Niu, Q., & Zhang, C. (2018b). Joint inversion of NMR and SIP data to estimate pore size distribution of geomaterials. *Geophysical Journal International*, *212*(3), 1791–1805. https://doi.org/10.1093/gji/ggx501

Niu, Q., & Zhang, C. (2019). Permeability prediction in rocks experiencing mineral precipitation and dissolution: A numerical study. *Water Resources Research*, *55*, 3107–3121. https://doi.org/10.1029/2018WR024174

O'Konski, C. T. (1960). Electric properties of macromolecules. V. Theory of ionic polarization in polyelectrolytes. *The Journal of Physical Chemistry*, *64*(5), 605–619.

Olhoeft, G. R. (1985). Low-frequency electrical properties. *Geophysics*, *50*(12), 2492–2503. https://doi.org/10.1190/1.1441880

Revil, A. (2012). Spectral induced polarization of shaly sands: Influence of the electrical double layer. *Water Resources Research*, *48*, W02517. https://doi.org/10.1029/2011WR011260

Revil, A. (2013). Effective conductivity and permittivity of unsaturated porous materials in the frequency range 1 mHz–1 GHz. *Water Resources Research*, *49*, 306–327. https://doi.org/10.1029/2012WR012700

Revil, A., Binley, A., Mejus, L., & Kessouri, P. (2015). Predicting permeability from the characteristic relaxation time and intrinsic formation factor of complex conductivity spectra. *Water Resources Research*, *51*, 6672–6700. https://doi.org/10.1002/2015WR017074

Revil, A., & Glover, P. W. J. (1998). Nature of surface electrical conductivity in natural sands, sandstones, and clays. *Geophysical Research Letters*, *25*(5), 691–694. https://doi.org/10.1029/98GL00296

Revil, A., Karaoulis, M., Johnson, T., & Kemna, A. (2012). Some low-frequency electrical methods for subsurface characterization and monitoring in hydrogeology. *Hydrogeology Journal*, *20*(4), 617–658. https://doi.org/10.1007/s10040-011-0819-x

Revil, A., Kessouri, P., & Torres-Verdín, C. (2014). Electrical conductivity, induced polarization, and permeability of the Fontainebleau sandstone. *Geophysics*, *79*(5), D301–D318. https://doi.org/10.1190/geo2014-0036.1

Revil, A., Koch, K., & Holliger, K. (2012). Is it the grain size or the characteristic pore size that controls the induced polarization relaxation time of clean sands and sandstones? *Water Resources Research*, *48*, W05602. https://doi.org/10.1029/2011WR011561

Revil, A., Meyer, C. D., & Niu, Q. (2016). A laboratory investigation of the thermoelectric effect. *Geophysics*, *81*(4), E243–E257. https://doi.org/10.1190/geo2015-0281.1

Rhoades, J. D., Raats, P. A. C., & Prather, R. J. (1976). Effects of liquid-phase electrical conductivity, water content, and surface conductivity on bulk soil electrical conductivity. *Soil Science Society of America Journal*, *40*(5), 651–655. https://doi.org/10.2136/sssaj1976.03615995004000050017x

Samet, M., Levchenko, V., Boiteux, G., Seytre, G., Kallel, A., & Serghei, A. (2015). Electrode polarization vs. Maxwell-Wagner-Sillars interfacial polarization in dielectric spectra of materials: Characteristic frequencies and scaling laws. *The Journal of Chemical Physics*, *142*(19), 194703.

Santamarina, J. C., Klein, K. A., & Fam, M. A. (2001). *Soils and waves*. New York: J. Wiley & Sons.

Schwarz, G. (1962). A theory of the low-frequency dielectric dispersion of colloidal particles in electrolyte solution. *The Journal of Physical Chemistry*, *66*(12), 2636–2642. https://doi.org/10.1021/j100818a067

Scott, J. B., & Barker, R. D. (2003). Determining pore-throat size in Permo-Triassic sandstones from low-frequency electrical spectroscopy. *Geophysical Research Letters*, *30*(9), 1450. https://doi.org/10.1029/2003GL016951

Sen, P. N., Scala, C., & Cohen, M. H. (1981). A self-similar model for sedimentary rocks with application to the dielectric constant of fused glass beads. *Geophysics*, *46*(5), 781–795. https://doi.org/10.1190/1.1441215

Sheng, P. (1990). Effective-medium theory of sedimentary rocks. *Physical Review B*, *41*(7), 4507. https://doi.org/10.1103/PhysRevB.41.4507

Sheng, P., & Callegari, A. J. (1984). Differential effective medium theory of sedimentary rocks. *Applied Physics Letters*, *44*(8), 738–740. https://doi.org/10.1063/1.94900

Shilov, V. N., Delgado, A. V., Gonzalez-Caballero, F., & Grosse, C. (2001). Thin double layer theory of the wide-frequency range dielectric dispersion of suspensions of non-conducting spherical particles including surface conductivity of the stagnant layer. *Colloids and Surfaces A: Physicochemical and Engineering Aspects*, *192*(1–3), 253–265. https://doi.org/10.1016/S0927-7757(01)00729-4

Streich, R. (2016). Controlled-source electromagnetic approaches for hydrocarbon exploration and monitoring on land. *Surveys in Geophysics*, *37*(1), 47–80. https://doi.org/10.1007/s10712-015-9336-0

Telford, W. M., Geldart, L. P., Sheriff, R. E., & Sheriff, R. E. (1990). *Applied geophysics*. Cambridge: Cambridge University Press. https://doi.org/10.1017/CBO9781139167932

Titov, K., Komarov, V., Tarasov, V., & Levitski, A. (2002). Theoretical and experimental study of time domain-induced polarization in water-saturated sands. *Journal of Applied Geophysics*, *50*(4), 417–433. https://doi.org/10.1016/S0926-9851(02)00168-4

Topp, G. C., Davis, J. L., & Annan, A. P. (1980). Electromagnetic determination of soil water content: Measurements in coaxial transmission lines. *Water Resources Research*, *16*(3), 574–582. https://doi.org/10.1029/WR016i003p00574

Topp, G. C., Yanuka, M., Zebchuk, W. D., & Zegelin, S. (1988). Determination of electrical conductivity using time domain reflectometry: Soil and water experiments in coaxial lines. *Water Resources Research*, *24*(7), 945–952. https://doi.org/10.1029/WR024i007p00945

Torquato, S. (2013). *Random heterogeneous materials: Microstructure and macroscopic properties* (Vol. 16). New York: Springer Science & Business Media.

Toumelin, E., & Torres-Verdín, C. (2007). 2D pore-scale simulation of wide-band electromagnetic dispersion of saturated rocks. *Geophysics*, *72*(3), F97–F110. https://doi.org/10.1190/1.2561301

Unsworth, M., Wenbo, W., Jones, A. G., Li, S., Bedrosian, P., Booker, J., et al. (2004). Crustal and upper mantle structure of northern Tibet imaged with magnetotelluric data. *Journal of Geophysical Research*, *109*, B02403. https://doi.org/10.1029/2002JB002305

Vaudelet, P., Revil, A., Schmutz, M., Franceschi, M., & Bégassat, P. (2011). Changes in induced polarization associated with the sorption of sodium, lead, and zinc on silica sands. *Journal of Colloid and Interface Science*, *360*(2), 739–752. https://doi.org/10.1016/j.jcis.2011.04.077

Volkmann, J., & Klitzsch, N. (2015). Wideband impedance spectroscopy from 1 mHz to 10 MHz by combination of four- and two-electrode methods. *Journal of Applied Geophysics*, *114*, 191–201. https://doi.org/10.1016/j.jappgeo.2015.01.012

Wardlaw, N. C., & McKellar, M. (1981). Mercury porosimetry and the interpretation of pore geometry in sedimentary rocks and artificial models. *Powder Technology*, *29*(1), 127–143. https://doi.org/10.1016/0032-5910(81)85011-5

Weller, A., & Slater, L. (2012). Salinity dependence of complex conductivity of unconsolidated and consolidated materials: Comparisons with electrical double layer models. *Geophysics*, *77*(5), D185–D198. https://doi.org/10.1190/geo2012-0030.1

Weller, A., Zhang, Z., Slater, L., Kruschwitz, S., & Halisch, M. (2016). Induced polarization and pore radius—A discussion. *Geophysics*, *81*(5), D519–D526. https://doi.org/10.1190/geo2016-0135.1

Yi, Z., Lin, M., Jiang, W., Zhang, Z., Li, H., & Gao, J. (2017). Pore network extraction from pore space images of various porous media systems. *Water Resources Research*, *53*, 3424–3445. https://doi.org/10.1002/2016WR019272

Zhan, X., Schwartz, L. M., Toksöz, M. N., Smith, W. C., & Morgan, F. D. (2010). Pore-scale modeling of electrical and fluid transport in Berea sandstone. *Geophysics*, *75*(5), F135–F142. https://doi.org/10.1190/1.3463704

Zhuravlev, L. T. (2000). The surface chemistry of amorphous silica. Zhuravlev model. *Colloids and Surfaces A: Physicochemical and Engineering Aspects*, *173*(1–3), 1–38. https://doi.org/10.1016/S0927-7757(00)00556-2